

Electron-capture decay rate of ^7Be in cluster and crystal forms of beryllium: A first-principles study

Riichi Kuwahara ^{*}

Dassault Systèmes K. K., ThinkPark Tower, 2-1-1 Osaki, Shinagawa-ku, Tokyo 141-6020, Japan

Kaoru Ohno [†]

Department of Physics, Yokohama National University, 79-5 Tokiwadai, Hodogaya-ku, Yokohama 240-8501, Japan

Tsutomu Ohtsuki [‡]

Institute for Integrated Radiation and Nuclear Science, Kyoto University, Asashiro-Nishi, Kumatori-cho, Sennan-gun, Osaka 590-0494 Japan



(Received 24 October 2023; accepted 22 January 2024; published 15 February 2024)

To discuss the half-life of the electron-capture decay of ^7Be in cluster and crystal forms of beryllium, we performed density functional calculations of the electron density $\rho(0)$ at the Be nucleus by assuming an inversely proportional relationship between them. We found that the electron density $\rho(0)$ decreases with cluster size in Be clusters and increases at an interstitial site in crystalline Be. The electron density $\rho(0)$ at the hexagonal close packed (HCP) lattice point, i.e., the substitutional site, is about 1.7% smaller than that at the center of C_{60} , which perfectly coincides with the recent experimental evidence [Phys. Rev. C **108**, L011301 (2023)] that the half-life of ^7Be in metallic Be at $T = 5\text{ K}$ is 1.7% longer than that of $^7\text{Be}@_{\text{C}_{60}}$ at $T = 5\text{ K}$ (i.e., at the center of C_{60}). This strongly suggests that at $T = 5\text{ K}$ all ^7Be stay at substitutional sites of the Be metal. For an interstitial Be atom, we found that the basal octahedral (BO) site is energetically most stable, and the basal split (BS) dumbbell structure is second most stable. Performing first-principles MD simulations of a system having an interstitial Be atom at room temperature, we found that (1) in a system having ^9Be atoms only, BO can quite rapidly migrate through BS; (2) BS made of ^7Be and ^9Be atoms very rapidly changes into BO of ^7Be ; and (3) ^7Be stays very stably at a BO site and seldom changes its position. Therefore, ^7Be stays more likely at BO than ^9Be at room temperature. The electron density $\rho(0)$ at BO is 0.54% higher than $\rho(0)$ at a substitutional site, which is about double the experimental difference of 0.26% in the half-life of ^7Be in Be metal between $T = 293\text{ K}$ and $T = 5\text{ K}$. This means that half of ^7Be atoms are at BO sites, but the other half still remain at substitutional sites at $T = 293\text{ K}$. So, we expect that the half-life of ^7Be can be further shortened at higher temperatures. Performing unit cell relaxation of a Be crystal, we found that the difference in the total energy between BO and BS is only 0.03 eV. Thus, if there is no ^7Be , BO can very easily migrate throughout the crystal through the $\text{BO} \rightarrow \text{BS} \rightarrow \text{BO}$ pathway at room temperature.

DOI: [10.1103/PhysRevC.109.024609](https://doi.org/10.1103/PhysRevC.109.024609)

I. INTRODUCTION

The electron-capture (EC) decay rate of a ^7Be nucleus has attracted considerable interest because it has recently been recognized that its value can significantly change according to its environment. By the EC decay reaction described as



(p , e^- , n , and ν_e are proton, electron, neutron, and neutrino, respectively), a ^7Be nucleus decays to a ^7Li nucleus. Segrè *et al.* first suggested that the EC decay rate should linearly depend on the electron density $\rho(0)$ at the ^7Be nucleus [1–3],

which enabled one to predict the EC decay rate from the first-principles calculation of the electron density. Even ^7Be nuclei have a finite size, and there is a volume overlap between the ^7Be nucleus and the s electrons where they can interact each other. The chemical environment may alter the s electron density $\rho(0)$ at the nucleus, and thus affect the EC decay rate. Hence the half-life is inversely proportional to the electron density $\rho(0)$ at the nucleus.

In previous studies, many experimental measurements and calculations were performed on the change in the half-life of ^7Be according to the host materials [4–13], chemical forms [14–18], and pressure [19,20]. Although, in most of these environments, the half-life of ^7Be was longer than 53.10 days (d), Ohtsuki *et al.* found, based on their experimental measurements supported by calculations, that the half-life of $^7\text{Be}@_{\text{C}_{60}}$ is $52.65 \pm 0.04\text{ d}$ at room temperature ($T = 293\text{ K}$) and $52.47 \pm 0.04\text{ d}$ at liquid-helium temperature

^{*}Riichi.KUWAHARA@3ds.com

[†]ohno@ynu.ac.jp

[‡]ohtsuki.tsutomu.d09@kyoto-u.jp

(just nearly $T = 5$ K) [21–23]. In these studies, the amount of radioactivity associated with the decay of ^7Be could uniquely be analyzed through the identification of characteristic γ rays ($E_\gamma = 478$ keV). Several calculations have further been performed to estimate the EC-decay rate of ^7Be encapsulated in C_{60} , C_{70} , and carbon nanotubes [24–28]. Quite recently, we performed both experiments and calculations [29] to show that the half-lives of $^7\text{Be}@C_{70}$ at room temperature ($T = 293$ K) and at liquid-helium temperature ($T = 5$ K) are comparable to or still slightly shorter than that of $^7\text{Be}@C_{60}$ at liquid-helium temperature ($T = 5$ K), which was previously thought to be the shortest half-life of ^7Be . In this paper, it was also reported that the half-life of ^7Be in a metallic Be is 53.39 ± 0.03 d at liquid-helium temperature ($T = 5$ K), which should be compared with 53.25 ± 0.04 d at room temperature ($T = 293$ K) [22,30]. This is about 0.26% difference. In this experiment, a $^9\text{Be}(\gamma, 2n)^7\text{Be}$ reaction in a pure Be crystal sample (by irradiating with a high energy γ -ray produced by bremsstrahlung of 50 MeV electrons under a magnetic field) was used to create ^7Be inside the Be crystal. The form of the emitted neutron spectrum is expected to be approximately Maxwellian, and the average neutron kinetic energy (KE) seems to be about 2–3 MeV, while the initial KE of the recoiled ^7Be nuclides can be estimated to be about a few hundred KeV even if the reaction is accompanied by two neutron emissions. Therefore, the ^7Be atoms being produced can escape from their original hexagonal close packed (HCP) structure due to the KE. The KE is reduced in the lattice with elastic and/or Coulomb multiple scattering and the radioactive ^7Be finally stop at interstitial sites. Then, the sample was baked in an electric oven with 1100°C for 1 hour and annealed after that to recover more stable lattice structure [21]. However, the ^7Be positions inside the Be metal were not determined experimentally.

The purpose of the present paper is to theoretically search various Be morphologies, which may exhibit drastic change in the half-life of ^7Be , and to theoretically elucidate the temperature dependence of the half-life of ^7Be in the Be metal, which was quite recently reported experimentally [29]. For this purpose, we systematically calculate the electron density $\rho(0)$ at the Be nucleus position in various cluster and crystal forms of beryllium using density functional theory (DFT) [31,32]. In the course of this study, we will clarify that the electron density $\rho(0)$ drastically changes according to the size of the Be cluster and also to the substitutional or interstitial sites in the Be crystal.

II. METHODOLOGY

In this study, we use the all-electron first-principles calculation program, DMol³ [33,34], which adopts numerical localized orbitals (on an atomic-centered spherical radial mesh) as basis functions in a linear combination of atomic orbitals (LCAO) approach. We use the double-numeric quality basis set with polarization functions (DNP). The size of the DNP basis set is comparable to Gaussian 6-31G**, but the numerical basis set is much more accurate than a Gaussian basis set of the same size to describe the cusplike behavior of the electron density near the nucleus. This is

the essential advantage in our calculations of $\rho(0)$. For the exchange-correlation (xc) functional, like our previous studies [22,23,25,29], we mainly employ the BLYP functional, which combines the exchange functional due to Becke [35] with the correlation functional of Lee-Yang-Parr [36], but we also employ the strongly constrained and appropriately normed meta-GGA functional (SCAN) [37] and the revised Tao, Perdew, Staroverov and Scuseria meta-GGA functional (revTPSS) [38]. One of the reasons that we chose the BLYP functional is that we have consistently chosen this functional throughout our previous papers [22,23,29]. Another reason is that this functional works excellently well for all our target systems (isolated Be atom, $\text{Be}@C_{60}$, and $\text{Be}@C_{70}$) as well as Be metals without problems. We have tested other functions as well. Table I lists the resulting electron density $\rho(0)$ at the Be nucleus position using a variety of exchange-correlation functionals, among which B3LYP, Minnesota M06(-2X), and SCAN0 are hybrid functionals, and -TS means Tkatchenko-Scheffler (TS) dispersion (van der Waals) correction [39]. From this table, we find that BLYP and B3LYP show a similar behavior, while Minnesota functionals (M06, M06-2X) and the strongly constrained and appropriately normed meta-GGA functionals (SCAN, SCAN0) show a somewhat different trend. Maybe this is related to the weaker performance of Minnesota functionals [40] and SCAN [41] for noncovalent or weakly bound compounds. Although B3LYP will slightly change the absolute value of $\rho(0)$, it is of limited significance, because only the relative changes of $\rho(0)$ are important for consideration.

In the crystal calculations, primitive cell and appropriate supercells as well as k -point samplings are used as described in the next section.

The interstitial migration path is determined using the FlexTS module [42–44] integrated with DMol³. FlexTS uses the doubly nudged elastic band method to obtain a reaction pathway, and then optimizes the energy maximum to obtain the transition state using the hybrid eigenvector following method. Once the transition state is found, the geometry optimization for plus and minus directions along the lowest Hessian eigenvector is performed to obtain the reactant and product for the reaction path. FlexTS automatically repeats this procedure until the reaction path connecting the reactant and product is achieved. First-principles MD (molecular dynamics) simulations at room temperature ($T = 293$ K) are also performed by DMol³ with the BLYP functional and a massive generalized Gaussian moments thermostat [45].

For the unit cell relaxation of the Be crystal with an interstitial atom, we use the CASTEP program [46] with the BLYP functional.

III. RESULTS AND DISCUSSION

A. Be Clusters

Structures of Be clusters have already been intensively investigated by many first-principles calculations [47–50]. We performed geometrical optimization starting from the structures given by Abyaz *et al.* [50] and estimated average nearest-neighbor (n.n.) bond length $\langle d \rangle$, total energy per atom

TABLE I. Functional dependence of $\rho(0)$ at the Be nucleus position for an atom, at the center of C_{60} , at the center of C_{70} , and at $X = 1.1$ Å from the center of C_{70} [29]. The small \pm values below the main values indicate the deviation from $\rho(0)$ of a Be atom.

	$\rho(0)$ (a.u.)							
	BLYP	BLYP-TS	B3LYP	B3LYP-TS	M06	M06-2X	SCAN	SCAN0
Be atom	35.953	35.953	35.692	35.695	35.816	35.837	35.797	35.825
Be@ C_{60}	36.016	36.019	35.772	35.773	35.868	35.820	35.826	35.862
center	+0.063	+0.066	+0.080	+0.078	+0.052	-0.017	+0.039	+0.037
Be@ C_{70}	35.990	35.990	35.737	35.737	35.822	35.767	35.787	35.819
center	+0.037	+0.037	+0.045	+0.042	+0.006	-0.070	-0.010	-0.006
Be@ C_{70}	36.007	36.009	35.760	35.761	35.819	35.818	35.823	35.856
$X = 1.1$ Å	+0.054	+0.056	+0.068	+0.066	+0.003	-0.019	+0.026	+0.031

E/N , spin state [singlet (S) or triplet (T)], Kohn-Sham energy eigenvalues of highest occupied molecular orbital (HOMO) and lowest unoccupied molecular orbital (LUMO) levels, average electron density $\rho(0)$ at the Be nucleus position, and its standard deviation $\Delta\rho(0)$ among all Be atoms in the cluster by using the BLYP functional. All these results are listed in Table II. The values E/N and $\rho(0)$ [$\Delta\rho(0)$], are in atomic units (a.u.), which are equal to Hartree (= 27.2114 eV) and

TABLE II. Calculated average nearest-neighbor bond length (d), total energy per atom E/N , spin state [singlet (S) or triplet (T)], Kohn-Sham energy eigenvalues of HOMO and LUMO levels, average electron density $\rho(0)$ at the Be nucleus position, and its standard deviation $\Delta\rho(0)$ among all Be atoms in Be clusters with size $N = 1-25$. (BLYP result.)

Size N	$\langle d \rangle$ (Å)	E/N (a.u.)	Spin (S/T)	HOMO (eV)	LUMO (eV)	$\rho(0)$ (a.u.)	$\Delta\rho(0)$ (a.u.)
1		-14.6581	S	-5.253	-1.191	35.953	
2	2.472	-14.6632	S	-4.164	-2.308	35.851	0.000
3	2.185	-14.6766	S	-4.436	-3.064	35.731	0.000
4	2.051	-14.6973	S	-4.800	-3.156	35.667	0.000
5	2.049	-14.7011	S	-4.009	-3.047	35.615	0.014
6	2.083	-14.7011	S	-3.586	-3.076	35.543	0.015
7	2.138	-14.7067	S	-4.096	-3.296	35.562	0.022
8	2.118	-14.7121	S	-4.006	-3.572	35.552	0.039
9	2.123	-14.7183	S	-4.260	-3.870	35.554	0.023
10	2.111	-14.7241	S	-4.267	-3.081	35.579	0.031
11	2.111	-14.7251	T	-3.904	-3.444	35.556	0.020
12	2.120	-14.7259	S	-4.159	-3.414	35.550	0.038
13	2.125	-14.7277	S	-4.127	-3.258	35.550	0.033
14	2.117	-14.7293	S	-4.120	-3.102	35.549	0.031
15	2.122	-14.7290	S	-3.779	-3.091	35.517	0.048
16	2.112	-14.7304	S	-4.416	-3.622	35.517	0.061
17	2.124	-14.7340	S	-4.570	-3.595	35.529	0.012
18	2.132	-14.7347	S	-4.243	-3.874	35.529	0.035
19	2.146	-14.7358	T	-4.398	-4.119	35.527	0.043
20	2.128	-14.7372	S	-4.584	-3.759	35.546	0.042
21	2.160	-14.7387	S	-4.582	-3.676	35.545	0.041
22	2.153	-14.7388	S	-4.416	-3.660	35.536	0.042
23	2.181	-14.7379	T	-4.586	-4.297	35.515	0.037
24	2.167	-14.7391	S	-4.716	-3.768	35.521	0.048
25	2.177	-14.7401	S	-4.513	-3.876	35.519	0.030

e^-/a_{B}^{-3} , respectively. The averaged n.n. bond length is large (2.472 Å) for the beryllium dimer Be_2 , as reported in previous studies [51,52], but it is shorter than its bulk value (2.285 Å; see later) for all other clusters Be_N ($N = 3-25$). The Kohn-Sham HOMO-LUMO energy gap is large in the Be atom and beryllium dimer Be_2 , but, for all other clusters there is no clear tendency versus the cluster size. Among other results, total energy per atom E/N and average electron density $\rho(0)$ at the Be nucleus position are plotted versus the cluster size N in Fig. 1. It is clearly seen in this figure that both total energy per atom E/N and average electron density $\rho(0)$ at the Be nucleus decrease with the cluster size. In particular, $\rho(0)$ decreases more rapidly between $N = 1$ and $N = 6$. There is a 1.2% difference in $\rho(0)$ between the Be atom and Be_6 , which indicates the 1.2% difference in the half-life of ${}^7\text{Be}$. We will see that $\rho(0) = 35.543$ a.u. of Be_6 and 35.519 a.u. of Be_{25} are already not so much different from the bulk value (see later) $\rho(0) = 35.517$ a.u. The difference is about 0.3%.

If we include the TS dispersion correction (BLYP-TS), $\rho(0)$ ($\langle d \rangle$) changes to 35.880 a.u. (2.743 Å) and 35.729 a.u. (2.223 Å) for Be_2 and Be_3 , respectively, although $\rho(0)$ of a Be atom does not change, as shown in Table I. However, $\rho(0)$ of larger clusters does not change much from its BLYP value.

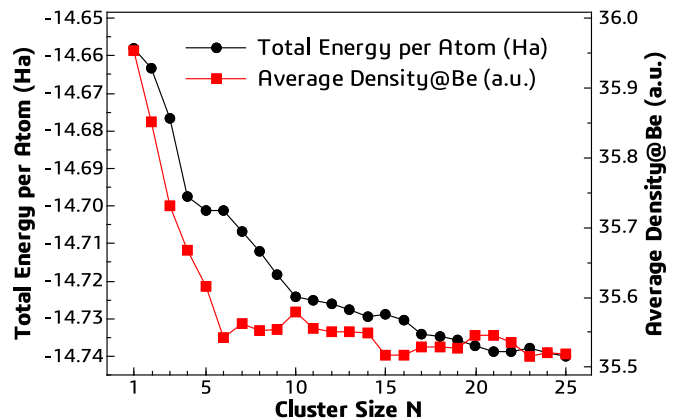


FIG. 1. Calculated total energy per atom E/N and average electron density $\rho(0)$ at the Be nucleus position versus the cluster size N ($= 1-25$). (BLYP result.)

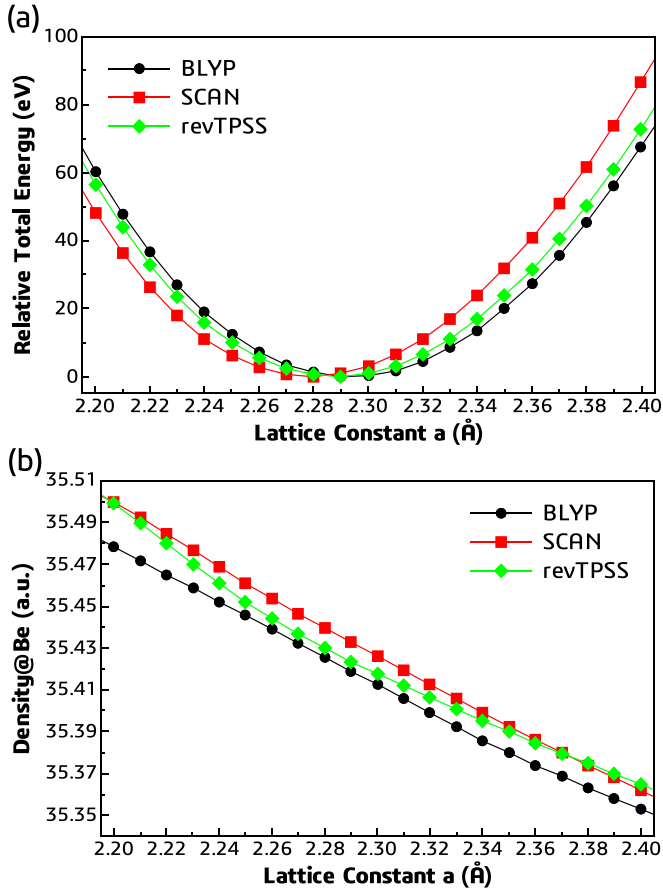


FIG. 2. (a) Relative total energy (eV) and (b) electron density $\rho(0)$ at the Be nucleus of Be crystal versus the lattice constant a (with c/a fixed at 1.569) calculated by using BLYP, SCAN, and revTPSS.

B. Perfect Be crystal

For the perfect Be crystal, we performed the HCP primitive cell calculation with $13 \times 13 \times 8$ k points. Figure 2(a) plots the total energy versus the lattice constant a (with c/a fixed at the experimental value 1.569 [53,54]) for different xc functionals: BLYP, SCAN, and revTPSS. As well, Fig. 2(b) plots the calculated electron density $\rho(0)$ at the Be nucleus position versus the lattice constant a . The electron density $\rho(0)$ slowly decreases with the lattice constant. Although the system is different, the EC decay rate is increased under pressure in BeO [19,20], which favors the present result. The electron density $\rho(0)$ at the optimized lattice constant is summarized in Table III. The optimized lattice constant is comparable to the previous results of first-principles calculations [55–59] as well as the experimental value of $a = 2.285$ and $c/a = 1.569$ [53,54]. Even if we use BLYP-TS with the same lattice constant of BLYP, the resulting $\rho(0) = 35.418$ a.u. is almost the same as $\rho(0) = 35.417$ a.u. of BLYP.

Since the thermal expansion coefficient of Be crystal is

$$\alpha = \frac{1}{a} \frac{da}{dT} = (5.0\text{--}11.1) \times 10^{-6} \text{ (K}^{-1}\text{)} \quad (2)$$

in the temperature region $T = -120\text{--}20$ °C [60], the lattice constant changes only 0.007 Å between absolute zero

TABLE III. Estimated electron density $\rho(0)$ (a.u.) at the Be nucleus at the optimized lattice constants, a (Å), c (Å), and c/a , in various xc functionals and experiments [53,54].

xc	a (Å)	c (Å)	$\frac{c}{a}$	$\rho(0)$ (a.u.)
BLYP	2.292	3.597	1.569	35.417
SCAN	2.275	3.584	1.575	35.440
revTPSS	2.282	3.606	1.580	35.424
experiments ^a	2.285	3.585	1.569	—

^aReferences [53,54].

temperature and room temperature, and there is no visible change in the electron density $\rho(0)$ at the Be nucleus in this temperature range.

By performing a first-principles MD simulation of a Be crystal at room temperature ($T = 293$ K), we found that the average electron density $\langle \rho(0) \rangle$ at the Be nucleus is increased to 35.426 a.u. at $T = 293$ K from 35.417 a.u. at $T = 0$ K as shown in Fig. 3. In this simulation, one of the stable nuclei ^9Be was replaced with radioactive ^7Be in the $3 \times 3 \times 2$ supercell; $\rho(0)$ of ^7Be is plotted with a red line and $\rho(0)$ of the remaining ^9Be is plotted with a black line in the figure. Although $\rho(0)$ of ^7Be becomes as large as 35.457 a.u. momentarily at $t = 2.7$ ps, its average value $\langle \rho(0) \rangle$ (horizontal red dashed line) is only very slightly larger than the average value $\langle \rho(0) \rangle$ of ^9Be (horizontal black dashed line); their difference is only in the fourth decimal place, which is less than the accuracy of the simulation.

Since the isolated Be trimer (Be_3) has a shorter bond length than the Be crystal and shows larger $\rho(0)$, one might expect a large temperature dependence of $\rho(0)$ by considering a shrinking oscillation of the basal regular three-membered rings (triangles) in the HCP crystal. To see if this is the case or not, we performed supercell calculations, in which one or all of the regular triangles (three-membered rings) are shrunk to the size of the Be_3 cluster, whose bond length is

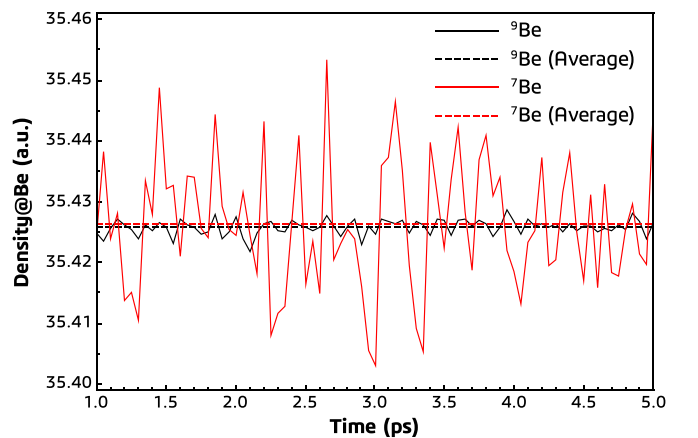


FIG. 3. Temporal change in electron densities $\rho(0)$ at the ^7Be nucleus (red line) and ^9Be nuclei (black line) during MD simulation at $T = 293$ K. Horizontal dashed lines represent their average values. (BLYP result).

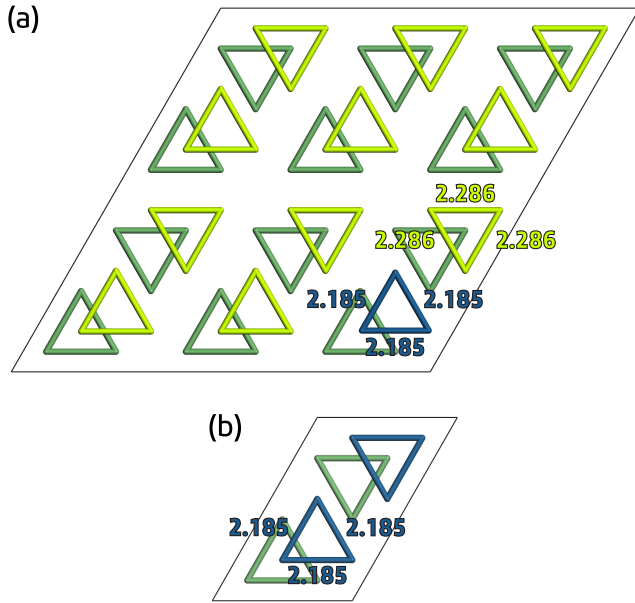


FIG. 4. Unit cells where (a) one triangle or (b) all triangles are replaced with that of a smaller isolated Be_3 in a perfect Be crystal with the original lattice constant fixed.

2.185 Å, which is shorter than the assumed bulk length of 2.286 Å by 0.1 Å. We used a $6 \times 6 \times 4$ supercell [including 288 atoms; see Fig. 4(a)] with $4 \times 6 \times 7$ k points and a $3 \times 2 \times 1$ supercell [including 12 atoms; see Fig. 4(b)] with $2 \times 2 \times 2$ k points, respectively, for one or all of the regular triangles with the shrunk size. All these assumed structures come back to the original regular HCP structure after relaxation, and they can be realized only through lattice vibrations. Although the isolated Be_3 cluster has $\rho(0) = 35.731$ a.u. (see Table II), the same Be_3 cluster embedded in the crystal has $\rho(0) = 35.430$ a.u., which is larger than $\rho(0) = 35.426$ of the perfect Be crystal at $T = 293$ K only by 0.037%, irrespective of the number of the shrunk three-membered rings in the HCP crystal. From these analyses, we think it is difficult to see any significant change in the value of $\rho(0)$ in the perfect Be crystal in the temperature range between absolute zero temperature and room temperature.

C. Interstitial Be atom in a crystal

Next, we consider an interstitial Be atom in a HCP crystal. For this calculation, we used $5 \times 5 \times 3$ supercell (including 151 atoms) with $3 \times 3 \times 2$ k points. For the “off-plane” interstitial sites out of the basal plane, we considered tetrahedral (T), octahedral (O), crowdion (C), and split (S) sites [61–65], where C is the center of an “off-plane” tetrahedral bond and S is the split dumbbell along the $\langle 0001 \rangle$ direction; see Fig. 5. For the interstitial sites in the basal plane, we considered basal tetrahedral (BT), basal octahedral (BO), basal crowdion (BC), and basal split (BS) sites [61–65], where BT and BO are the centers of basal triangles of a tetrahedron and octahedron, respectively, BC is the center of a bond of a basal triangle, and BS is the basal split dumbbell along the $\langle 11\bar{2}0 \rangle$ direction in the basal plane; see Fig. 5. We found that BO

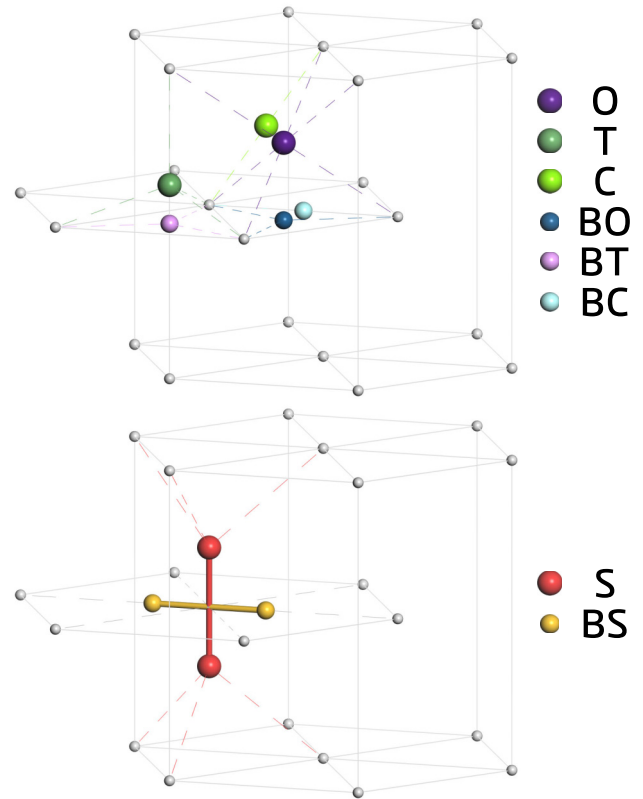


FIG. 5. Eight conventional interstitial sites in HCP crystal. Tetrahedral (T), octahedral (O), crowdion (C), basal tetrahedral (BT), basal octahedral (BO), and basal crowdion (BC) sites in the upper panel, and split (S) and basal split (BS) sites in the lower panel.

is the energetically most stable interstitial site and BS is the second most stable geometry. BC is unstable and moved to BO after relaxation. These results are all in accordance with the previous first-principles study by Ganchenkova *et al.* [63]. Moreover, by performing a transition state (TS) search using FlexTS (see the previous section), we found that there are transition barriers between BS and BO [Fig. 6(a)] and between C and BO [Fig. 6(b)]. The energy difference between BO and BS is 0.064 eV, corresponding to 6.2 kcal/mol, and the transition barrier height measured from the BO level is 0.069 eV. The electron density $\rho(0)$ at the Be nucleus decreases from 35.610 a.u. at BO to 35.586 a.u. at BS; the difference is only 0.06%. Similarly, the energy difference between BO and C is 0.093 eV and the barrier height from the BO level is 0.190 eV, while the electron density $\rho(0)$ changes around 35.57–35.62 a.u. The octahedral interstitial site O itself is the saddle point in the path $\text{BO} \rightarrow \text{BO}$, as shown in Figs. 6(c) and 7. The results are listed in Table IV. The magnitude of the displacement (from the lattice point) of neighboring atoms (NAs) around the interstitial atom is $\Delta d = 0.484$ Å for three NAs around BO; $\Delta d = 0.283$ Å for six NAs around O; and $\Delta d = 0.973$ Å for one NA, 0.398 Å for two NAs, 0.307 Å for two NAs, and smaller than 0.150 Å for one NA around BS.

We found that the interstitial Be atom is energetically most stable at BO, which is depicted as a large blue ball in Fig. 7(a). In this figure, there are also six side nonregular

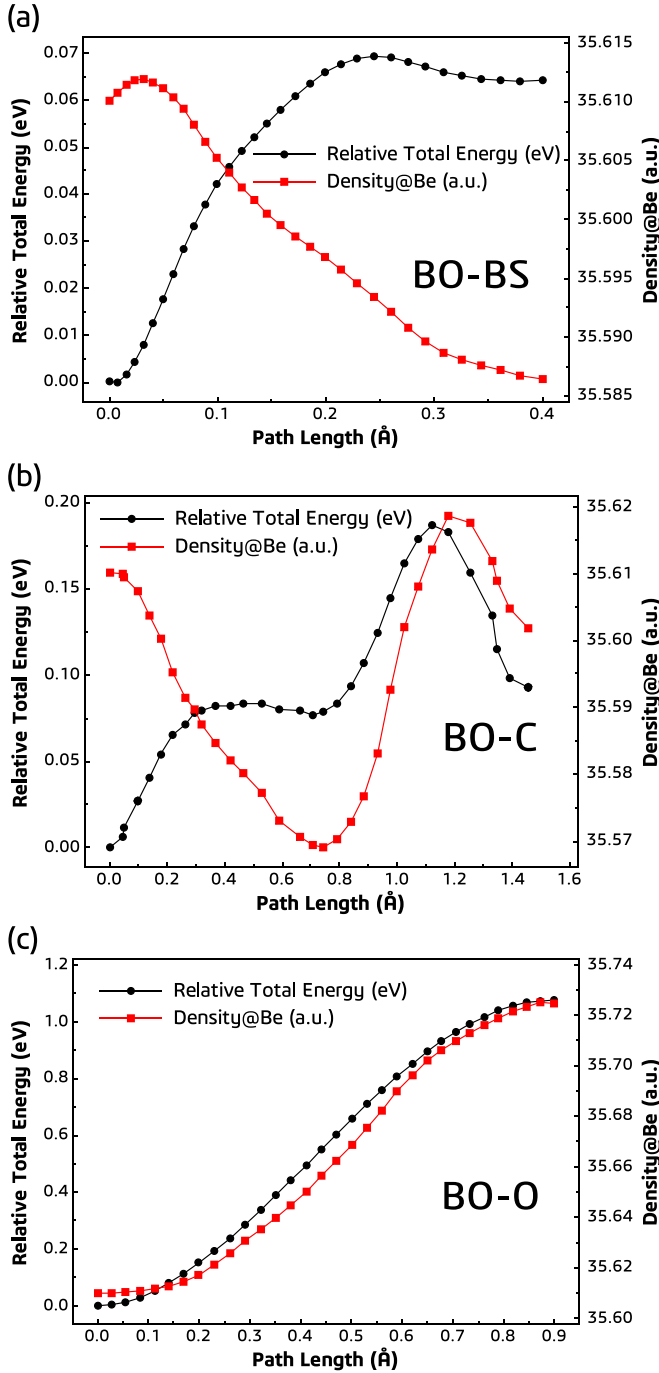


FIG. 6. Change in the relative (total) energy and the electron density $\rho(0)$ at the Be nucleus along the migration path coordinates (a) from BO (path length 0) to BS (path length 0.4 Å), (b) from BO (path length 0) to the crowdion site C (path length 1.45 Å), and (c) from BO (path length 0) to the octahedral interstitial site O (path length 0.9 Å), which is a saddle point. (BLYP result).

triangles besides upper and lower regular triangles in the octahedron composed of the six middle-sized moss green Be atoms. However, the positions at the center of these nonregular triangles are all unstable and the Be atom put there moves to the most stable interstitial sites at the upper or lower BO after relaxation. Moreover, from the TS search, we found that

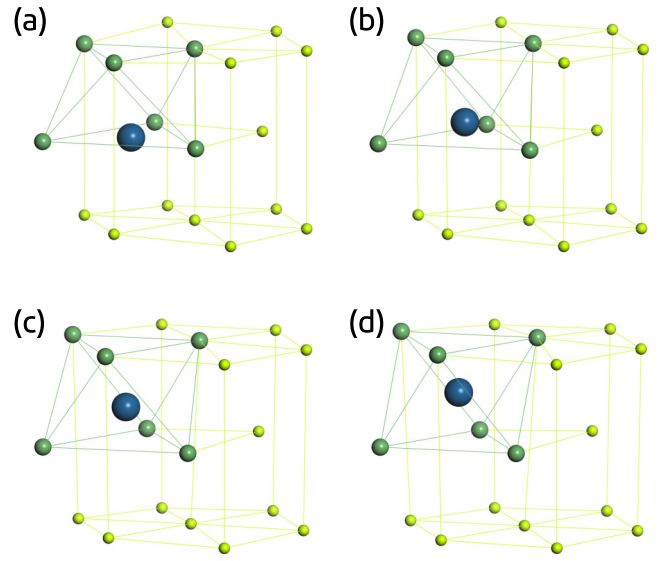


FIG. 7. Migration path of the large blue interstitial atom from (a) BO, through (b) and (c), toward (d) the octahedral interstitial site O, which is the saddle point, determined by the transition state search using FlexTS. Six middle-sized moss green atoms represent an octahedron.

the octahedral site O [Fig. 7(d)] is not the metastable site but the saddle point (transition state) in the path between the lower and upper BO sites; see Fig. 7. The total energy and the electron density $\rho(0)$ at the Be nucleus change along this migration path as shown in Fig. 6(c). The energy difference between these two points (BO and O) is about 1.1 eV, which corresponds to 25 kcal/mol. The electron density $\rho(0)$ at the Be nucleus increases from 35.610 a.u. at BO to 35.725 at O, which is about 0.33% difference. To depict the difference in the charge density distribution between the interstitial Be atom and the isolated Be atom, the total electron density is subtracted by the following two densities: (i) density of a system without the interstitial atom, and (ii) density of a

TABLE IV. Estimated electron density $\rho(0)$ (a.u.) at the Be nucleus which is located at various interstitial sites (BO, BS, BC, C, T, S, O, and BT) together with its total energy relative to BO. Note that BC is unstable and moved to BO after relaxation. The relative total energy of the transition state (TS) toward BO is also shown in the third column. O itself is the saddle point (TS) in the path BO \rightarrow BO. (BLYP result.)

Site	Relative total energy (eV)	Energy of TS toward BO (eV)	$\rho(0)$ (a.u.)
BO	0.000		35.610
BS	0.064	0.069	35.586
BC	unstable (relax to BO)		
C	0.093	0.190	35.602
T	0.990		35.584
S	1.075		35.600
O	1.077	saddle point	35.725
BT	1.587		35.654

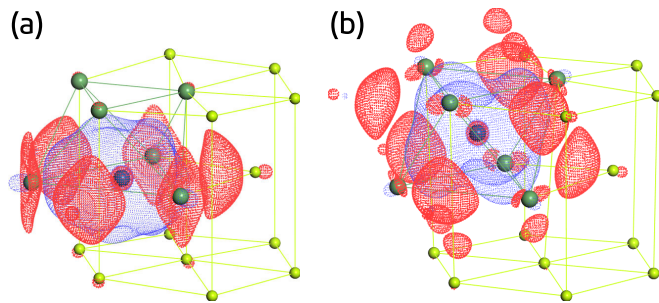


FIG. 8. Difference in the electron density when the interstitial atom is at (a) BO and (b) O. The blue (e^-) and red (e^+) isosurface values are $\pm 0.02 \text{ \AA}^{-3}$.

system composed of the interstitial atom only, i.e., almost the isolated Be atom. The result is shown in Fig. 8, where the electron rich and poor regions are represented, respectively, in blue and red colors. The difference in the electron density near the center of the interstitial atom is negative, i.e., electron poor and red, because $\rho(0) = 35.610$ a.u. or 35.725 at the interstitial site (BO or O) is smaller than $\rho(0) = 35.953$ of an isolated Be atom; see Tables II and IV. Almost the amount of one electron is accumulated around the interstitial atom (blue region). This means that electrons are confined in the narrow interstitial region compared with a widely spread out electron distribution of an isolated atom. The electron depletion region around it (red region) represents the tail of the electron distribution of an isolated atom. The red region located at six surrounding islands is somewhat larger when the interstitial atom is located at BO [Fig. 8(a)] compared to the case when it is at O [Fig. 8(b)], while there are many small remote red islets in the latter case. This reflects the electron density distribution being narrowly compressed on the basal plane but widely spread out in the direction perpendicular to the basal plane at the BO site, whereas there is an almost isotropically compressed electron density distribution in the O site. This is probably the reason for the higher electron density $\rho(0)$ at the nuclear position at the O site. That is, the interstitial O region is more compressed from all directions and corresponds to the circumstance in the compressed lattice constant of the Be crystal, in which $\rho(0)$ becomes higher as shown in Fig. 2(b).

We performed two different first-principles MD simulations of a Be crystal ($5 \times 5 \times 3$ supercell) including one interstitial Be atom at room temperature ($T = 293$ K) for a period of 5 ps using DMol³ with the BLYP functional.

The first simulation is for a system consisting of ${}^9\text{Be}$ atoms only, and starts from the optimized geometry with one BO as shown in Fig. 9(a). Soon, at 1.8 ps, this BO involves a Be atom at the adjacent lattice point, becoming BS as shown in Fig. 9(b). Then, at 2.0 ps, this newly included Be atom remains at BO and the other Be atom, which originally constituted the initial BO (large ball), comes back to the nearest lattice point as shown in Fig. 9(c). In this way, the BO site moves from the original position to the adjacent position through the intermediate BS geometry. Since this movement of BO frequently happens in the simulation, we conclude that a rapid migration of BO through BS may occur at room temperature. The second simulation is for a system consisting of all ${}^9\text{Be}$ except one ${}^7\text{Be}$,

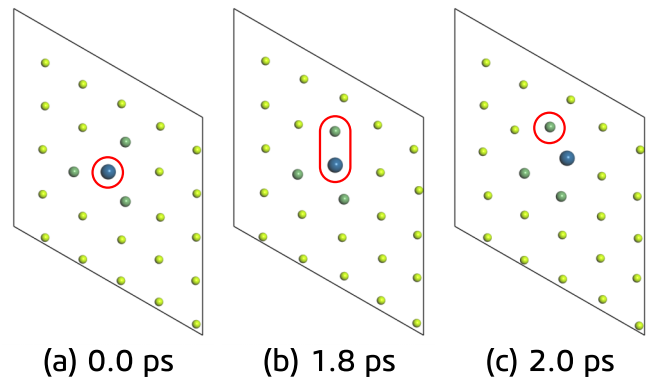


FIG. 9. Snapshots of MD of a system consisting of all ${}^9\text{Be}$ showing a rapid migration of BO through BS: (a) initial (optimized) BO at 0 fs, (b) BS by including upper Be in the dumbbell at 1.8 ps, and (c) BO of the upper Be, leaving the lower Be to the lattice point, at 2.0 ps.

and starts from the optimized geometry with one BS made up of a ${}^7\text{Be}$ atom and a ${}^9\text{Be}$ atom as shown in Fig. 10(a). Very quickly, at 0.3 ps, the ${}^9\text{Be}$ atom (medium ball) moves from BS to a lattice point as shown in Fig. 10(b). Then, at 0.5 ps, the other ${}^7\text{Be}$ (large ball) remains at BO as shown in Fig. 10(c). However, after the BO of ${}^7\text{Be}$ is created, the geometry does not change during the simulation. We performed another MD simulation starting from a geometry having a BO of ${}^7\text{Be}$ in the Be crystal, and confirmed that this is a very stable geometry and there is no change in the geometry during the simulation period of 5 ps. Thus we find that, at room temperature, BS very quickly changes into BO which consists of ${}^7\text{Be}$ and is locationally very stable.

IV. DISCUSSION

In the half-life measurement of ${}^7\text{Be}$ in a metallic Be done by Ohtsuki *et al.* [29], the ${}^9\text{Be}(\gamma, n){}^7\text{Be}$ reaction was used to create ${}^7\text{Be}$ inside the Be crystal. In this reaction, high energy ${}^7\text{Be}$ atoms are created with neutron emissions, repeat many

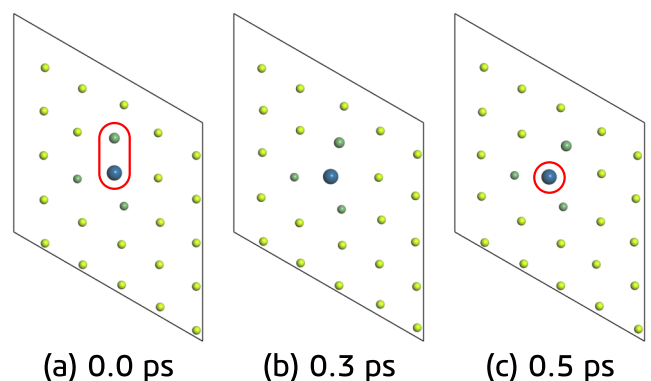


FIG. 10. Snapshots of MD of a system consisting of ${}^9\text{Be}$ (small and medium balls) except one ${}^7\text{Be}$ (large ball): (a) initial (optimized) BS made up of ${}^7\text{Be}$ and ${}^9\text{Be}$ at 0 fs, (b) ${}^9\text{Be}$ moving from BS to a lattice point at 0.3 ps, and (c) ${}^7\text{Be}$ remaining at BO at 0.5 ps.

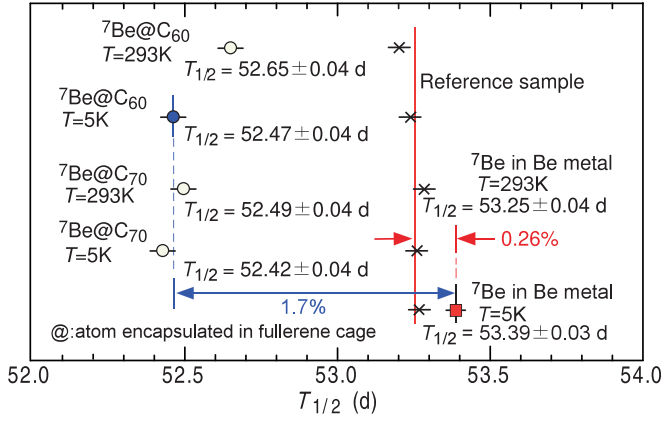


FIG. 11. Half-life of ${}^7\text{Be}$ experimentally measured by Ohtsuki *et al.* (after Ref. [29]).

elastic scatterings, and finally stop at certain positions inside the Be metal. Although the sample was baked in an electric oven at 1100°C for 1 hour and annealed after that to recover a more stable lattice structure [21], there is a large possibility that interstitial atoms still remain in the metal [66,67].

The half-life of ${}^7\text{Be}$ in the Be metal at liquid-helium temperature ($T = 5\text{ K}$) is $53.39 \pm 0.03\text{ d}$, which is about 1.7% longer than the half-life $52.47 \pm 0.04\text{ d}$ of ${}^7\text{Be}@C_{60}$ at liquid-helium temperature ($T = 5\text{ K}$) [22] and 0.26% longer than the half-life $53.25 \pm 0.04\text{ d}$ in the Be metal at room temperature ($T = 293\text{ K}$); see Fig. 11. Now, we will discuss a possibility of explaining these experimental facts using our BLYP results.

First, we calculated the Frenkel defect formation energy by using DMol³ with the BLYP functional. We assumed that a Frenkel defect is made of one BO and one atomic vacancy. When the distance between BO and vacancy is infinite, the Frenkel defect formation energy can be determined by the equation [68]

$$\Delta E_{\text{defect}} = E_{\text{BO}}^{(N+1)} + E_{\text{vacancy}}^{(N-1)} - 2E_{\text{crystal}}^{(N)}, \quad (3)$$

where $E_{\text{BO}}^{(N+1)}$, $E_{\text{vacancy}}^{(N-1)}$, and $E_{\text{crystal}}^{(N)}$ are the total energies of an $(N+1)$ -atom system with one BO, an $(N-1)$ -atom system with one vacancy, and an N -atom system of a perfect crystal, respectively. The Frenkel defect formation energy in this case is estimated as 4.62 eV. When BO and vacancy are located on the same basal plane and their distance is about 6.62 \AA as shown in Fig. 12(a), the Frenkel defect formation energy is 4.43 eV. When BO and vacancy are located on different, adjacent basal planes and their distance is about 3.91 \AA as shown in Fig. 12(b), the Frenkel defect formation energy is 4.31 eV, which is comparable to the previous result of 4.2 eV [63]. When BO and vacancy are put closer to each other, they merge to recover a perfect crystal or the local geometry of BO is broken after relaxation. Thus, comparing the resulting Frenkel defect formation energy with the thermal energy of order $\sim k_{\text{B}}T$, we conclude that Frenkel defects in the Be crystal cannot be created by the thermal fluctuation at room temperature, but can only be created by the initial ${}^9\text{Be}(\gamma, 2n){}^7\text{Be}$ reaction. Thus, in the following discussion,

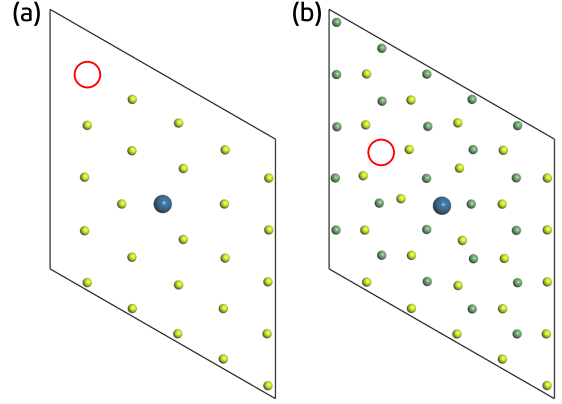


FIG. 12. Frenkel defect made of one BO (large blue ball) and one atomic vacancy (red circle) (a) on the same basal plane and (b) on different, adjacent basal planes. In (b), small light green and moss green balls are atoms on the different basal planes.

we assume that some interstitial atoms already exist in the Be crystal by construction.

From Table III, the electron density at the HCP lattice point, i.e., the substitutional site, is $\rho(0) = 35.417\text{ a.u.}$, which is about 1.7% different from the value $\rho(0) = 36.016$ at the center of C_{60} (Table I) [23,29]. This is perfectly coincident with the 1.7% difference in the half-life of ${}^7\text{Be}$ at $T = 5\text{ K}$ between $53.39 \pm 0.03\text{ d}$ of the Be metal and $52.47 \pm 0.04\text{ d}$ of ${}^7\text{Be}@C_{60}$ (at the center of C_{60}) [29]. Therefore, we conclude that at $T = 5\text{ K}$ all ${}^7\text{Be}$ are at the substitutional site of the Be crystal. This conclusion seems statistically quite reasonable, because the numbers of ${}^7\text{Be}$ atoms and interstitial atoms are both very limited compared to the vast numbers of ${}^9\text{Be}$ atoms and substitutional sites in the Be metal.

On the other hand, from our MD simulations having an interstitial atom at room temperature, the 0.26% difference in the half-life of ${}^7\text{Be}$ in the Be crystal between $T = 5\text{ K}$ and $T = 293\text{ K}$ may be explained as follows. First, from the first conclusion above, we can readily see that $\rho(0)$ of ${}^7\text{Be}$ in the Be metal at $T = 5\text{ K}$ is equal to $\rho(0)$ at the substitutional site. When all the atoms are ${}^9\text{Be}$, a rapid migration of BO through BS occurs at room temperature, as shown in Fig. 9. When one of the atoms is ${}^7\text{Be}$, which constitutes BS together with another ${}^9\text{Be}$, this BS changes quite rapidly into the BO of ${}^7\text{Be}$ as shown in Fig. 10. This BO of ${}^7\text{Be}$ is locationally very stable and seldom changes its position. From these results, it is clear that ${}^7\text{Be}$ stays at BO with higher possibility than ${}^9\text{Be}$ at room temperature. This is an isotope effect. Concerning the action and reaction due to the interatomic force between ${}^7\text{Be}$ and ${}^9\text{Be}$ constituting BS, the acceleration of ${}^7\text{Be}$ is $9/7$ times larger than that of ${}^9\text{Be}$. Therefore, ${}^7\text{Be}$ prefers looser space than ${}^9\text{Be}$, and keeps staying at BO by pushing ${}^9\text{Be}$ back to the HCP substitutional site, which is tightly surrounded by 12 n.n. atoms. From Table IV, we find $\rho(0) = 35.610\text{ a.u.}$ at BO, which should be compared with $\rho(0) = 35.417\text{ a.u.}$ at the substitutional site. This is 0.54% difference, which is about double the experimental difference of 0.26%. However, we do not know what percentage of ${}^7\text{Be}$ are located at BO at $T = 293\text{ K}$. If we assume that all ${}^7\text{Be}$ are located at BO

at $T = 293$ K, then the calculated 0.54% difference obviously does not explain the experimental 0.26% difference. Now, we use the key point that $\rho(0)$ of ${}^7\text{Be}$ in the Be metal can be estimated by the weighted average of $\rho(0) = 35.610$ a.u. at BO and $\rho(0) = 35.417$ a.u. at the substitutional site with the weights proportional to the respective populations of ${}^7\text{Be}$ at BO and at the substitutional site. To match the experimental 0.26% difference, we are led to the second conclusion that, at $T = 293$ K, 48% of ${}^7\text{Be}$ are located at BO and 52% of ${}^7\text{Be}$ are located at the substitutional site. Then, we can successfully reproduce the experimental 0.26% difference as $0.48 \times 0.54\% = 0.26\%$. That is, although we could not identify only from our calculation what percentage of ${}^7\text{Be}$ are located at BO at $T = 293$ K, the comparison between the calculated 0.54% and the experimental 0.26% enabled us to conclude that 48% of ${}^7\text{Be}$ are located at BO and the remaining 52% are located at the substitutional site at $T = 293$ K. However, this does not necessarily mean that all the atoms filling the BO sites are ${}^7\text{Be}$ isotopes only. Needless to say, there are many other BO sites filled by ${}^9\text{Be}$ atoms as well.

(The half-life of ${}^7\text{Be}$ in metallic Be at room temperature was first reported as 53.12 ± 0.06 d in the earlier work of Ohtsuki *et al.* earlier work [21,69], and then modified to a more reliable 53.25 ± 0.04 d in their later work by the measurements of repetition [22,29,30]. Although this earlier value might not be suitable, we can still theoretically justify it, because it is different from 53.39 ± 0.03 d at $T = 5$ K [29] by 0.51%, which is slightly less than 0.54%, and the ${}^7\text{Be}$ atoms can be considered to be mostly at BO sites in this sample).

In order to check the effect of unit cell relaxation, we performed unit cell relaxation of the Be crystal with an interstitial atom by using the CASTEP program with the BLYP functional. The total energies of BO (without symmetry) and BS (with symmetry) are, respectively, $-59\,239.897$ eV and $-59\,239.864$ eV, and the difference between them is 0.03 eV. (Such a small energy difference between different interstitial sites under the cell relaxation has been found in the HCP zirconium system also [65]). This result strongly supports our conclusion that BO can easily migrate throughout the crystal through the $\text{BO} \rightarrow \text{BS} \rightarrow \text{BO}$ pathway, if there is no ${}^7\text{Be}$ in the crystal.

V. SUMMARY

Since ${}^7\text{Be}$ nuclei have a finite size, there is a net volume overlap between the ${}^7\text{Be}$ nucleus and the s electrons where they can interact each other. The chemical environment may alter the s electron density $\rho(0)$ at the nucleus and thus affect the EC decay rate. In this paper, by assuming the inverse proportionality between the half-life and the electron density $\rho(0)$ at the ${}^7\text{Be}$ nucleus position, we have systematically calculated the latter in Be_n ($n = 1-25$) clusters and in Be crystals by using density functional theory.

In the case of clusters, the value of $\rho(0)$ quite rapidly decreases from $n = 1$ to $n = 6$, and its value of Be_6 is already close to its bulk value; the difference is only 0.3%. On the other hand, in a perfect single Be crystal, the value of $\rho(0)$

hardly changes in the temperature range between absolute zero temperature and room temperature either by thermal expansion or by lattice vibration. The electron density at the HCP lattice point, i.e., the substitutional site, is about 1.7% smaller than that at the center of C_{60} , which perfectly coincides with the experimental evidence [29] that the half-life of ${}^7\text{Be}$ of the Be crystal at $T = 5$ K is 1.7% longer than that of ${}^7\text{Be}@C_{60}$ at $T = 5$ K (i.e., at the center of C_{60}). Thus, we are led to the first conclusion that at $T = 5$ K all ${}^7\text{Be}$ are at the substitutional site of the Be crystal.

Next, we considered an interstitial Be atom in a Be crystal. The energetically most stable interstitial position is the basal octahedral (BO) site, while the octahedral interstitial (O) site is the transition state on the path between two facing BO sites. According to our BLYP result, the energy difference is 1.1 eV (25 kcal/mol) and the electron density difference $\Delta\rho(0)$ is about 0.33% between the BO and the O sites. The second most stable interstitial site is the basal split (BS) site. The energy difference is 0.064 eV (6.2 kcal/mol) and the electron density difference $\Delta\rho(0)$ is only 0.06% between the BO and BS sites.

We performed MD simulations of a system having an interstitial Be atom at room temperature, and found that (1) in a system with ${}^9\text{Be}$ atoms only, BO can quite rapidly migrate through BS; (2) BS made of ${}^7\text{Be}$ and ${}^9\text{Be}$ atoms very rapidly changes into BO of ${}^7\text{Be}$; and (3) ${}^7\text{Be}$ stays very stably at a BO site and seldom changes its position. Thus, we expect that ${}^7\text{Be}$ stays more likely at BO than ${}^9\text{Be}$ at room temperature. The electron density $\rho(0)$ at BO is 0.54% higher than $\rho(0)$ at the substitutional site, which is about double the experimental difference of 0.26% [29] in the half-life of ${}^7\text{Be}$ between $T = 293$ K and $T = 5$ K. This brings us the second conclusion that half of the ${}^7\text{Be}$ atoms are at the BO sites, but the other half remain at the substitutional sites at $T = 293$ K, which again perfectly explains the experiment. So, we expect that the half-life of ${}^7\text{Be}$ can be further shortened at higher temperatures.

We have also performed unit cell relaxation of the Be crystal and found that difference in the total energy between BO and BS is only 0.03 eV. This result strongly supports the statement that BO can very easily migrate throughout the crystal through the $\text{BO} \rightarrow \text{BS} \rightarrow \text{BO}$ pathway at room temperature if there is no ${}^7\text{Be}$ in the crystal.

Finally, in our calculation, the Frenkel defect formation energy is 4.62 eV when the distance between BO and vacancy is infinite, and decreases to 4.31 eV when the distance is 3.91 Å.

We conclude that first-principles studies of the structure, electron density, and formation energies greatly help us quantitatively understand the EC decay rate of ${}^7\text{Be}$ in various morphologies of beryllium as well as the diffusion and migration of interstitial atoms in beryllium crystals.

ACKNOWLEDGMENTS

This work was supported by Japan Society of Promotion of Science (JSPS) Grants-in-Aid for Scientific Research, KAKENHI (No. 21H01877 and No. 19K22596).

- [1] E. Segrè, *Phys. Rev.* **71**, 274 (1947), (Minutes of the Meeting, Contributed Papers, A3).
- [2] E. Segrè and C. E. Wiegand, *Phys. Rev.* **75**, 39 (1949).
- [3] R. F. Leininger, E. Segrè, and C. Wiegand, *Phys. Rev.* **76**, 897 (1949).
- [4] F. Lagoutine, J. Legrand, and C. Bac, *Int. J. Appl. Radiat. Isot.* **26**, 131 (1975).
- [5] M. Jaeger, S. Wilmes, V. Kölle, G. Staudt, and P. Mohr, *Phys. Rev. C* **54**, 423 (1996).
- [6] A. Ray, P. Das, S. K. Sasha, S. K. Das, B. Sethi, A. Mookerjee, C. B. Chaudhuri, and G. Pari, *Phys. Lett. B* **455**, 69 (1999).
- [7] E. B. Norman, G. A. Rech, E. Browne, R. M. Larimer, M. R. Dragowsky, Y. D. Chan, M. C. P. Isaac, R. J. McDonald, and A. R. Smith, *Phys. Lett. B* **519**, 15 (2001).
- [8] A. Ray, P. Das, S. K. Sasha, and S. K. Das, *Phys. Lett. B* **531**, 187 (2002).
- [9] L. Zhi-Yi, C.-B. Li, S.-G. Wang, J. Zhou, Q.-Y. Meng, S.-J. Lu, and S.-H. Zhou, *Chin. Phys. Lett.* **20**, 829 (2003).
- [10] B. N. Limata, Z. Fülöp, D. Schürmann, N. D. Cesare, A. D'Onofrio, A. Esposito, L. Gialanella, G. Gyürky, G. Imbriani, F. Raiola, V. Roca, D. Rogalla, C. Rolfs, M. Romano, E. Somorjai, F. Strieder, and F. Terrasi, *Eur. Phys. J. A* **27**, 193 (2006).
- [11] Y. Nir-El, G. Haquin, Z. Yungreiss, M. Hass, G. Goldring, S. K. Chamoli, B. S. N. Singh, S. Lakshmi, U. Köster, N. Champault, A. Dorsival, G. Georgiev, V. N. Fedoseyev, B. A. Marsh, D. Schumann, G. Heidenreich, and S. Teichmann, *Phys. Rev. C* **75**, 012801(R) (2007).
- [12] B. N. Limata, L. Gialanella, A. D. Leva, N. D. Cesare, A. D'Onofrio, G. Gyurky, C. Rolfs, M. Romano, D. Rogalla, C. Rossi, M. Russo, E. Somorjai, and F. Terrasi, *Nucl. Instrum. Methods Phys. Res. Sect. B* **266**, 2117 (2008).
- [13] V. Kumar, M. Hass, Y. Nir-El, G. Haquin, and Z. Yungreiss, *Phys. Rev. C* **77**, 051304(R) (2008).
- [14] P. Benoist, R. Bouchez, P. Daudel, R. Daudel, and A. Rogozinski, *Phys. Rev.* **76**, 1000 (1949).
- [15] H. W. Johlige, D. C. Aumann, and H. J. Born, *Phys. Rev. C* **2**, 1616 (1970).
- [16] C.-A. Huh, *Earth Planet. Sci. Lett.* **171**, 325 (1999).
- [17] J. A. Tossell, *Earth Planet. Sci. Lett.* **195**, 131 (2002).
- [18] K. K. M. Lee and G. Steinle-Neumann, *Earth Planet. Sci. Lett.* **267**, 628 (2008).
- [19] W. K. Hensley, W. A. Bassett, and J. R. Huizenga, *Science* **181**, 1164 (1973).
- [20] A. Ray, P. Das, A. K. Sikdar, S. Pathak, N. Aquino, M. Lozano-Espinosa, and A. N. Artemyev, *Eur. Phys. J. D* **75**, 140 (2021).
- [21] T. Ohtsuki, H. Yuki, M. Muto, J. Kasagi, and K. Ohno, *Phys. Rev. Lett.* **93**, 112501 (2004).
- [22] T. Ohtsuki, K. Ohno, T. Morisato, T. Mitsugashira, K. Hirose, H. Yuki, and J. Kasagi, *Phys. Rev. Lett.* **98**, 252501 (2007).
- [23] T. Morisato, K. Ohno, T. Ohtsuki, K. Hirose, M. Sluiter, and Y. Kawazoe, *Phys. Rev. B* **78**, 125416 (2008).
- [24] E. V. Tkalya, A. V. Bibikov, and I. V. Bodrenko, *Phys. Rev. C* **81**, 024610 (2010).
- [25] S. Ono, R. Kuwahara, T. Morisato, and K. Ohno, *Chem. Phys. Lett.* **561-562**, 137 (2013).
- [26] A. V. Bibikov, A. V. Nikolaev, and E. V. Tkalya, *Phys. Rev. C* **100**, 064603 (2019).
- [27] F. Gholamian, M. M. Firoozabadi, and H. Raissi, *Phys. Rev. C* **102**, 014606 (2020).
- [28] A. Yoshida, M. Abe, and M. Hada, *J. Phys. Chem. A* **125**, 6356 (2021).
- [29] T. Ohtsuki, R. Kuwahara, and K. Ohno, *Phys. Rev. C* **108**, L011301 (2023).
- [30] T. Ohtsuki, K. Ohno, T. Morisato, and K. Hirose, *Mater. Trans.* **48**, 646 (2007).
- [31] P. Hohenberg and W. Kohn, *Phys. Rev.* **136**, B864 (1964).
- [32] W. Kohn and L. J. Sham, *Phys. Rev.* **140**, A1133 (1965).
- [33] B. Delley, *J. Chem. Phys.* **92**, 508 (1990).
- [34] B. Delley, *J. Chem. Phys.* **113**, 7756 (2000).
- [35] A. D. Becke, *J. Chem. Phys.* **88**, 2547 (1988).
- [36] C. Lee, W. Yang, and R. G. Parr, *Phys. Rev. B* **37**, 785 (1988).
- [37] J. Sun, A. Ruzsinszky, and J. P. Perdew, *Phys. Rev. Lett.* **115**, 036402 (2015).
- [38] J. P. Perdew, A. Ruzsinszky, G. I. Csonka, L. A. Constantin, and J. Sun, *Phys. Rev. Lett.* **103**, 026403 (2009).
- [39] A. Tkatchenko and M. Scheffler, *Phys. Rev. Lett.* **102**, 073005 (2009).
- [40] N. Mardirossian and M. Head-Gordon, *J. Chem. Theory Comput.* **12**, 4303 (2016).
- [41] E. B. Isaacs and C. Wolverton, *Phys. Rev. Mater.* **2**, 063801 (2018).
- [42] Y. Kumeda, D. J. Wales, and L. J. Munro, *Chem. Phys. Lett.* **341**, 185 (2001).
- [43] S. A. Trygubenko and D. J. Wales, *J. Chem. Phys.* **120**, 2082 (2004).
- [44] J. M. Carr, S. A. Trygubenko, and D. J. Wales, *J. Chem. Phys.* **122**, 234903 (2005).
- [45] R. Windiks and B. Delley, *J. Chem. Phys.* **119**, 2481 (2003).
- [46] S. J. Clark, M. D. Segall, C. J. Pickard, P. J. Hasnip, M. I. J. Probert, K. Refson, and M. C. Payne, *Z. Kristallogr.* **220**, 567 (2005).
- [47] J. Wang, G. Wang, and J. Zhao, *J. Phys.: Condens. Matter* **13**, L753 (2001).
- [48] S. Srinivas and J. Jellinek, *J. Chem. Phys.* **121**, 7243 (2004).
- [49] V. Cerowski, B. K. Rao, S. K. Khanna, P. Jena, S. Ishii, K. Ohno, and Y. Kawazoe, *J. Chem. Phys.* **123**, 074329 (2005).
- [50] B. Abyaz, Z. Mahdaviifar, G. Schreckenbach, and Y. Gao, *Phys. Chem. Chem. Phys.* **23**, 19716 (2021).
- [51] J. M. Merritt, V. E. Bondybey, and M. C. Heaven, *Science* **324**, 1548 (2009).
- [52] P. Reinhardt, J. Toulouse, and A. Savin, *Theor. Chem. Accounts* **137**, 168 (2018).
- [53] V. M. Amonenko, V. Ye. Ivanov, G. F. Tikhinskii, and V. A. Finkel, *Fiz. Met. Metalloved.* **14**, 128 (1962) [*Phys. Met. Metallogr.* **14**, 114 (1962)].
- [54] K. J. H. Mackay and N. A. Hill, *J. Nucl. Mater.* **8**, 263 (1963).
- [55] R. Dovesi, C. Pisani, F. Ricca, and C. Roetti, *Phys. Rev. B* **25**, 3731 (1982).
- [56] M. Y. Chou and P. K. Lam, and M. L. Cohen, *Phys. Rev. B* **28**, 4179 (1983).
- [57] G. V. Sin'ko and N. A. Smirnov, *Phys. Rev. B* **71**, 214108 (2005).
- [58] F. Luo, L.-C. Cai, X.-R. Chen, F.-Q. Jing, and D. Alfè, *J. Appl. Phys.* **111**, 053503 (2012).
- [59] A. Dal Corso, *J. Phys.: Condens. Matter* **28**, 075401 (2016).

- [60] P. Hidnert and W. T. Sweeney, *Sci. Papers Bur. Stand.* **22**, 533 (1927).
- [61] R. A. Johnson and J. R. Beeler, in *Interatomic Potentials and Crystalline Defects*, edited by J. K. Lee (The Metallurgical Society of AIME, New York, 1981), pp. 165–179.
- [62] D. J. Bacon, *J. Nucl. Mater.* **159**, 176 (1988).
- [63] M. G. Ganchenkova, P. V. Vladimirov, and V. A. Borodin, *J. Nucl. Mater.* **386-388**, 79 (2009).
- [64] A. Tunde Raji, S. Scandolob, R. Mazzarello, S. Nsengiyumva, M. Härtinga, and D. T. Britton, *Philos. Mag.* **89**, 1629 (2009).
- [65] Q. Peng, W. Ji, J. Lian, X.-J. Chen, H. Huang, F. Gao, and S. De, *Sci. Rep.* **4**, 5735 (2014).
- [66] C.-H. Woo, in *Radiation-Induced Changes in Microstructure: 13th International Symposium (Part I)*, ASTM STP 955, edited by F. A. Garner, N. H. Packan, and A. S. Kumar (ASTM, Philadelphia, 1997), pp. 70–89.
- [67] P. F. Lugakov and T. A. Lukashevich, *Phys. Status Solidi A* **110**, 403 (1988).
- [68] M. I. Shutikova and V. V. Stegailov, *J. Phys.: Condens. Matter* **34**, 475701 (2022).
- [69] T. Ohtsuki, H. Yuki, J. Kasagi, and M. Muto, *Prog. Theor. Phys. Suppl.* **154**, 392 (2004).